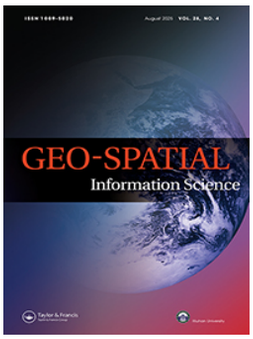

Taylor & Francis
Taylor & Francis Group

Geo-spatial Information Science

ISSN: 1009-5020 (Print) 1993-5153 (Online) Journal homepage: www.tandfonline.com/journals/tgsi20

Shadow-constrained shape-from-shading for pixel-wise 3D surface reconstruction at the lunar south pole

Ranye Jia, Bo Wu, Wai Chung Liu, Yue Peng, Sergey Krasilnikov, Liyan Sheng & Song Peng

To cite this article: Ranye Jia, Bo Wu, Wai Chung Liu, Yue Peng, Sergey Krasilnikov, Liyan Sheng & Song Peng (2025) Shadow-constrained shape-from-shading for pixel-wise 3D surface reconstruction at the lunar south pole, Geo-spatial Information Science, 28:4, 1880-1898, DOI: 10.1080/10095020.2024.2386978

To link to this article: https://doi.org/10.1080/10095020.2024.2386978

Published online: 15 Aug 2024.

GEO-SPATIAL INFORMATION SCIENCE
2025, VOL. 28, NO. 4, 1880–1898
https://doi.org/10.1080/10095020.2024.2386978

Shadow-constrained shape-from-shading for pixel-wise 3D surface reconstruction at the lunar south pole

Ranye Jia[a], Bo Wu[a], Wai Chung Liu[a], Yue Peng[a], Sergey Krasilnikov[a], Liyan Sheng[b] and Song Peng[b]

[a]Planetary Remote Sensing Laboratory, Department of Land Surveying & Geo-Informatics, The Hong Kong Polytechnic University, Hong Kong, China; [b]Institute of Spacecraft System Engineering, China Academy of Space Technology, Beijing, China

ABSTRACT

High-resolution digital elevation models (DEMs) of the lunar surface are crucial for lunar exploration missions and scientific research. The emergence of advanced technologies, such as Shape-from-Shading (SfS), has enabled the generation of pixel-wise high-resolution DEMs from monocular images of the lunar surface. However, SfS encounters significant challenges in locations with limited illumination, such as the lunar south pole, where the surface is largely covered by shadows. Therefore, this paper presents a novel shadow-constrained SfS approach for pixel-wise 3D surface reconstruction at the lunar south pole. The proposed approach uses multiple high-resolution images captured under different illumination conditions and an existing low-resolution DEM as the inputs and generates a high-resolution DEM with the same resolution as that of the input image through hierarchical SfS processing incorporating shadow constraints. Experiments were conducted using actual images collected by the Lunar Reconnaissance Orbiter (LRO) Narrow Angle Camera (NAC) at the lunar south pole. Comparisons with respect to photogrammetric DEMs generated from stereo NAC images show that the DEMs generated using the proposed approach exhibit the smallest root mean square error (RMSE). Moreover, shaded relief images rendered from the DEMs generated using the proposed approach demonstrate the highest similarity to the actual NAC images. Detailed profile comparisons further validate the effectiveness of the shadow constraint in optimizing 3D reconstruction in regions in proximity to shadows and within shadowed regions. The proposed shadow-constrained SfS approach can be used to generate high-resolution DEMs to support future missions to explore the lunar south pole, with applications including landing site evaluation and route planning for lunar probes or astronauts.

ARTICLE HISTORY
Received 11 January 2024
Accepted 27 July 2024

KEYWORDS
Lunar south pole; surface reconstruction; DEM; shape-from-shading; shadow

1. Introduction

Digital Elevation Models (DEMs) of the lunar surface are typically obtained through laser altimetry (Smith et al. 2010) or stereo photogrammetry (Di et al. 2014; Wu, Hu, and Guo 2014). Laser altimetry can yield highly accurate DEMs. However, the large sample spacing results in low spatial resolution. Photogrammetry uses stereo image pairs to generate DEMs with resolutions 3–10 times (Heipke et al. 2007; Wu, Zhang, and Zhu 2012) those of the input images, depending on the abundance of image textures. High-resolution stereo images (0.5–1.5 m/pixel) captured by the Lunar Reconnaissance Orbiter (LRO) Narrow Angle Camera (NAC) have been widely used for generating DEMs in the past (Speyerer et al. 2016; Tran et al. 2010; Wu and Liu 2017). However, at the lunar south pole, where the solar elevation angles are generally low (e.g. maximum solar elevation of ~ 2° at the south pole, 90°S), severe shadows are cast across the surface and on the images. This phenomenon renders dense image matching in photogrammetry challenging, resulting in significant problems (e.g. holes due to missing data and interpolation defects) in DEMs generated for the lunar south pole (Rosiek et al. 2013).

Shape-from-Shading (SfS) is a photometry-based surface reconstruction method that reconstructs 3D geometry (shape) based on the relationships between the image intensity (shading), illumination, and viewing directions (Horn 1977; Tsai and Shah 1994; Wu et al. 2018). SfS can recover pixel-wise surface shapes from a single image (Grumpe, Belkhir, and Wöhler 2014; Wu et al. 2018) or multiple images (Liu, Wu, and Wöhler 2018). With existing low-resolution DEMs generated either from laser altimetry or photogrammetry serving as the initial control, SfS algorithms have successfully been used for pixel-wise 3D surface reconstruction at the Chang'E-4 and Chang'E-5 landing regions on the Moon (Liu and Wu 2020; Wu, Li, et al. 2020) and on Mars (Hess et al. 2022; Liu and Wu 2023). However, the performance of SfS deteriorates

CONTACT Bo Wu bo.wu@polyu.edu.hk;

in areas with significant shadows, such as the lunar south pole, and SfS itself cannot reconstruct 3D information within the shadows.

Shape-from-Shadow is a technology used to reconstruct 3D information based on terrain geometry and illumination information (Mamassian 2014). Shape-from-Shadow differs from SfS by focusing on the geometric relationship between the shadowed and illuminated areas instead of the luminance information in pixels. Nevertheless, shadow information can provide useful constraints for enhancing SfS reconstruction, especially in regions in proximity to shadows. Therefore, this study is aimed at developing a shadow-constrained SfS method to address shadow-related challenges for 3D surface reconstruction at the lunar south pole.

The rest of the paper is organized as follows. Section 2 presents a review of related work. Section 3 describes the shadow-constrained SfS approach in detail. Section 4 outlines experimental evaluations of the proposed method, conducted using LRO NAC images collected at the lunar south pole. Section 5 presents the conclusions and discussion.

2. Related work

SfS algorithms were initially developed for surface reconstruction of close-range scenes in the computer vision field (Horn 1977, 1990). Kirk (1987) presented the earliest use of SfS for 3D reconstruction of planetary surfaces. SfS estimates the 3D surface based on the photometric relationship between the radiance information on the image and the surface slopes. It estimates the surface slope of each pixel in the image based on a photometric model (McEwen 1991) and reconstructs the underlying 3D surface to re-produce the image. SfS can effectively generate detailed pixel-wise 3D models even from a single image (Dulova et al. 2008; Wu et al. 2018). Typically, the SfS method is underdetermined, which implies that a single input image may correspond to multiple viable 3D shapes (Horn 1977; Tsai and Shah 1994). In this case, additional information such as existing low-resolution DEM (Wu et al. 2018) or multiple images acquired under different illumination conditions (Liu, Wu, and Wöhler 2018; Woodham 1980) may be used to introduce constraints to achieve optimal results.

The performance of SfS algorithms is considerably affected by the reflecting ability of the surface (i.e. albedo). Although the assumption of a constant albedo, which has been adopted in various studies, can simplify the process, it results in unavoidable defects (Horn 1990; Lohse & Heipke 2004). While some studies (Alexandrov and Beyer 2018; Grumpe, Belkhir, and Wöhler 2014; Hess et al. 2022; Korokhin et al. 2018; Li et al. 2021; Liu and Wu 2020; Wu et al. 2018) have allowed varying albedo in the SfS process, this has necessitated additional constraints, such as those pertaining to existing low-resolution DEMs, to facilitate solution convergence. Notably, when multiple images captured under different illumination conditions are available (Liu, Wu, and Wöhler 2018), each image can serve as an observation. By synergistically integrating these observations, more precise estimates of shape and albedo can be derived (Chandraker et al. 2007). Alexandrov and Beyer (2018) presented an SfS approach using multiple images and a coarse-resolution DEM. The approach can recover more topographic details than those obtained from monocular images, and the coarse-resolution DEM provides overall topographic constraints and improves the geometric accuracy. However, this strategy requires the availability of multiple images covering the same area, captured under different illumination conditions. Although SfS methods have been successfully used for 3D reconstruction of the lunar surface in the past decade (Grumpe, Belkhir, and Wöhler 2014; Liu and Wu 2020; Wu et al. 2018, 2021), their use for 3D surface reconstruction at the lunar south pole has remained limited owing to severe shadows in the region.

Stereophotoclinometry (SPC) is a reliable approach for 3D surface reconstruction (Gaskell 2004, 2008) that improves upon the limitations of the SfS method. SPC is a combination of stereo photogrammetry and photoclinometry, capable of generating high-accuracy and high-resolution DEMs from multiple images (Gaskell et al. 2008). The SPC technique obtains absolute surface elevations using stereo photogrammetry and relies on photoclinometry to refine the spatial resolution of the final DEM (Palmer et al. 2016). In recent years, deep-learning-based methods have been developed for 3D surface reconstruction. For instance, Chen, Wu, and Liu (2021) refined a coarse-resolution DEM to obtain a high-resolution DEM using a well-trained Convolutional Neural Network (CNN). Chen et al. (2022) attempted to enhance the recovery of topographic details by incorporating photoclinometry into deep-learning-derived DEMs. Liu et al. (2022) presented a deep-learning-based method for pixel-wise DEM generation using deep neural networks and demonstrated promising performance. Tao et al. (2023) generated high-resolution lunar DEMs using an in-house deep-learning model. However, deep-learning methods typically require large training datasets, which are difficult to obtain. At the lunar south pole, extremely low illumination poses significant challenges for 3D surface reconstruction, and difficulties such as obtaining favorable training datasets for deep-learning-based methods are more pronounced.

Shape-from-Shadow represents a promising technique for estimating the 3D shape of a surface by analyzing the shadow geometry in the scene (Daum & Dudek 1998; Shafer and Kanade 1983). In this approach, the shadowed portion of an image is

delineated, and the objects (e.g. crater rims or mountains) casting the shadows are identified. The geometric relationship between the objects casting the shadows and shadowed region is solved based on the illumination incidence and azimuth angles. With the aid of multiple images captured under different illumination conditions, the surface shape can be jointly solved using the shadow-inferred geometric relationship. Shadows can pose challenges for 3D reconstruction using SfS algorithms. However, they can provide useful geometric information to constrain SfS algorithms, thereby enhancing their performance. Therefore, this paper introduces a shadow-constrained SfS approach for 3D surface reconstruction at the lunar south pole.

3. Shadow-constrained SfS for pixel-wise 3D surface reconstruction

3.1. Overview of the proposed approach

The proposed shadow-constrained SfS approach is aimed at enhancing the elevation reconstruction of the SfS algorithm in regions near shadows and within shadowed regions, where the SfS algorithm is not adequately effective. Multiple NAC images captured under different illumination conditions are used as inputs, and a low-resolution LOLA DEM (20 m/pixel) serves as the initial control, inherited from our previous SfS method (Wu et al. 2018). The shadow-constrained SfS model involves two steps: estimation of elevations from each image using the SfS method (Liu and Wu 2023; Wu et al. 2018) and optimization of the elevation in regions in proximity to shadows and within shadows. Figure 1 shows the framework of the shadow-constrained SfS approach.

With a low-resolution DEM as the initial control, the input images are resampled to the same resolution (e.g. 20 m/pixel) as that of the initial DEM. The SfS method is then used to reconstruct elevations for the illuminated pixels. The SfS algorithm continuously processes the incoming image data, iteratively calculating elevation values for each pixel until the elevation estimates converge. Upon convergence, each elevation value associated

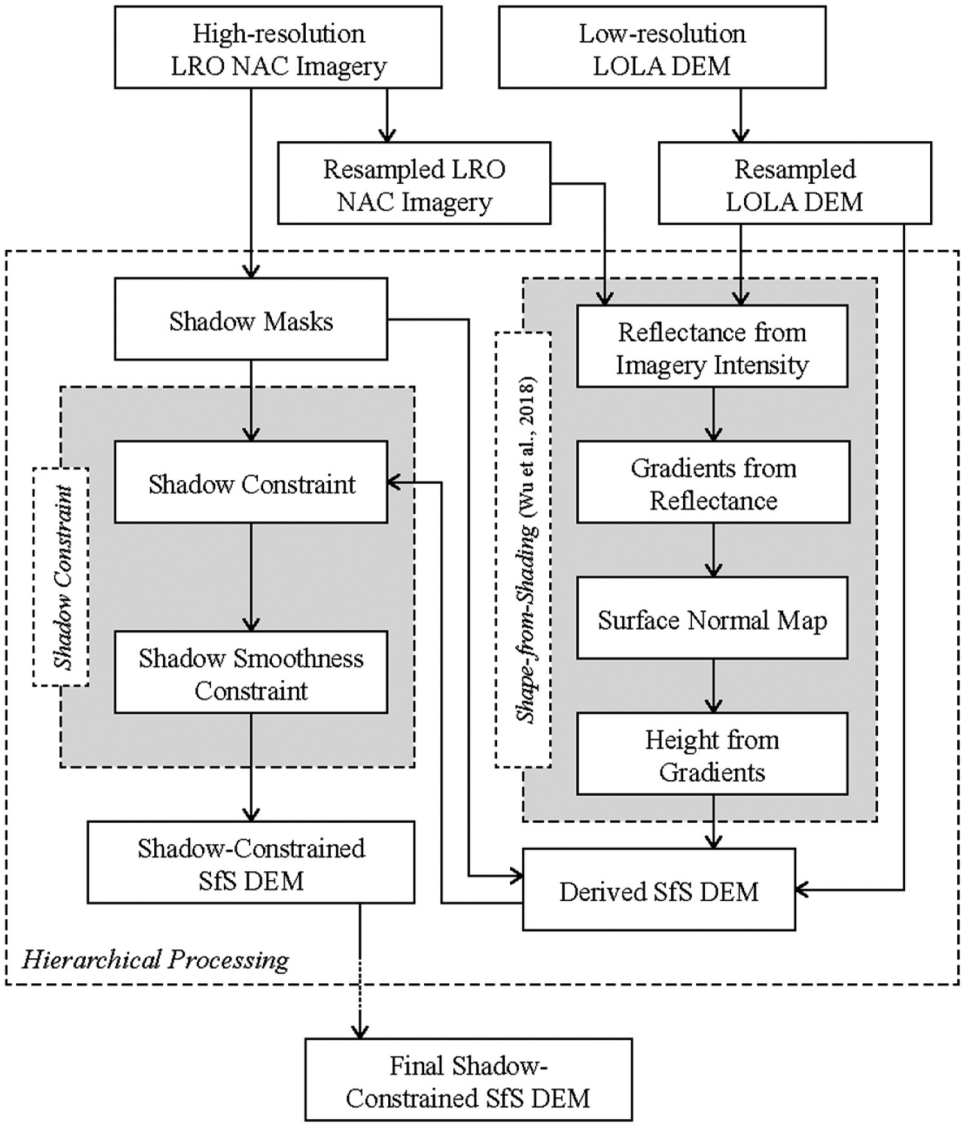

Figure 1. Framework of the shadow-constrained SfS approach.

with a pixel represents the outcome of jointly considering both the luminance and elevation corresponding to the relevant region within the input image and low-resolution DEM. In other words, the elevation value for any pixel that has been illuminated at least once is optimized using the SfS algorithm with reference to the low-resolution DEM. In shadowed regions, where pixels are covered by shadows in the input NAC image, the SfS method adheres to the initial input elevation values. Subsequently, an SfS DEM is generated, which serves as the input for the processing of all other NAC images.

Following SfS processing, the SfS DEM is fed to the shadow constraint module for enhancement. The shadow constraint module calculates corrections to the SfS DEM based on each input NAC image. After one iteration, the corrected shadow-constrained SfS DEM and input NAC images are resampled to a higher resolution (i.e. 10 m/pixel) and introduced in the workflow for similar processing. This optimization processing is hierarchically conducted until the resolution of the images and DEMs reaches the predefined value (i.e. the same resolution as the NAC image).

3.2. Shadow-constrained SfS model

The shadow-constrained SfS hierarchical optimization involves two steps: (1) SfS processing and (2) shadow-constrained processing. The SfS module iteratively refines the DEM using pixel-wise intensities of the high-resolution image, based on the following reflectance model.

$$I = A \times G(p, q) \tag{1}$$

Equation (1) describes the relationship between the image intensity, surface reflecting properties (i.e. albedo A), and reflectance $G(p, q)$ produced by the topography. The reflectance model $G(p, q)$ relates the surface gradients (p, q), illumination conditions, and image intensity through a mathematic equation. Although various reflectance models are available, the lunar – Lambert model (McEwen 1991) is used in this study owing to its simplicity.

A and G for each pixel are initialized using the input DEM and image. Then, G is iteratively adjusted using optimization strategies similar to those used in our previous methods (Liu and Wu 2020; Wu et al. 2018). The DEM is optimized as:

$$E_{img} = \left(G_{sfs} - G_{\mathrm{DEM}}\right)^2 \tag{2}$$

where G_{sfs} refers to the SfS-adjusted G, and G_{DEM} refers to G produced by the input DEM.

The input DEM also serves as a coarse-resolution constraint for the SfS process:

$$E_{\mathrm{DEM}} = \left[g(Z_{ini}, \sigma) - g\left(Z_{sfs}, \sigma\right)\right]^2 \tag{3}$$

where Z_{ini} refers to the input DEM, Z_{sfs} denotes the DEM under SfS processing, and $g(*, \sigma)$ represents a Gaussian smoothing operator with σ as the predefined standard deviation.

As the elevation information in areas in proximity to shadows and within the shadows may not be accurately reconstructed through the abovementioned processing, a shadow constraint is introduced to correct the elevations as follows:

$$E_{SHD} = \left[Z_{SfS} - Z_{SHD}\right]^2 \tag{4}$$

where Z_{SHD} is the estimated elevation from the shadow constraint. Equation (4) indicates that the elevations derived from the SfS process should be adjusted to match those attained from the shadow constraint.

Combining all terms mentioned above, the complete error equation can be formulated as

$$E_{\mathrm{Total}} = E_{img} + w_{\mathrm{DEM}} E_{\mathrm{DEM}} + E_{SHD} \tag{5}$$

where w_{DEM} is the weight controlling the contribution of the input DEM. The reconstruction process is optimized using Equation (5), based on a relaxation approach (Wu et al. 2018). The process initiates from the input resolution (i.e. the resolution of the initial DEM). After each iteration, the resulting DEM and images are up-sampled to the resolution at the next pyramid level (e.g. half the resolution at the previous level), yielding a DEM with the same resolution as that of the up-sampled data. Optimization processing continues until the resolution reaches the pre-defined value (i.e. the same resolution as the NAC image).

3.3. Shadow constraint

The shadow constraint is based on an illumination-shadow model of a 2D profile. A hypothetical light source is assumed to emit parallel light with a known direction. The 2D illumination-shadow model is based on a terrain profile and assumed to be oriented in the same direction as the light rays in the horizontal plane, as shown in Figure 2(a). The topography surface profile along the direction of illumination is divided into three parts: $x_1 - x_2$, which is illuminated by a light source placed on the upper left side; $x_2 - x_3$, which is partially occluded by the peak, corresponding to point x_2; and $x_3 - x_4$, which is illuminated again on the right side of point x_3, away from the light source. The elevation difference ΔH between the shadow occlusion point x_2 and shadow boundary point x_3 is calculated using the horizontal distance between these two points and the altitude angle of solar illumination.

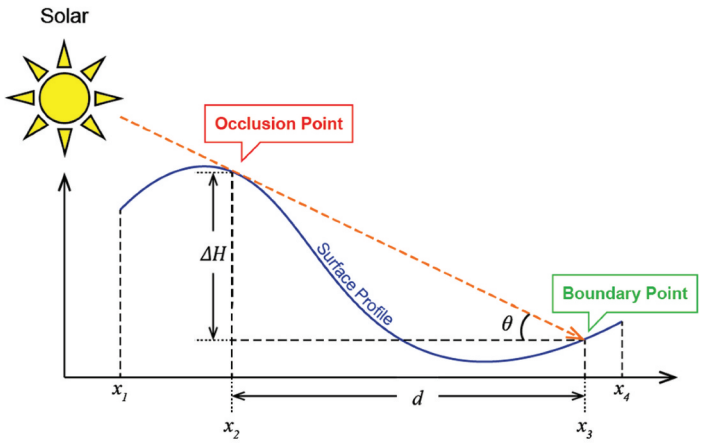

(a) Determination of ΔH through shadow constraint in a 2D profile.

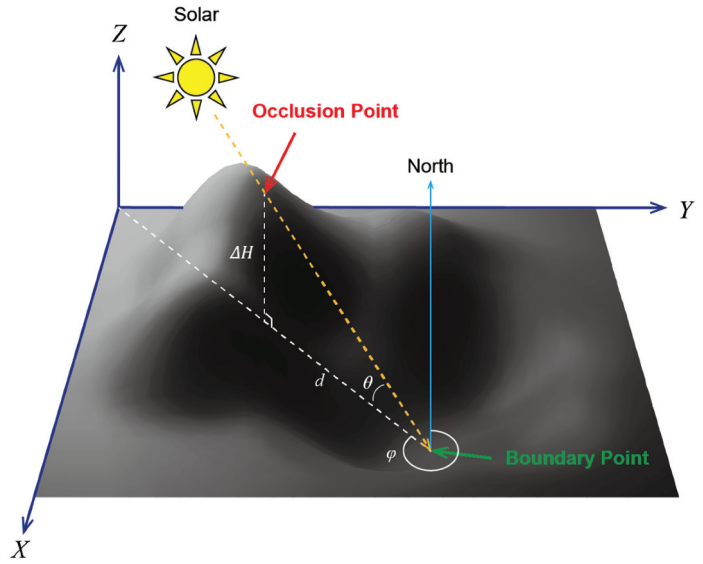

(b) Determination of ΔH through shadow constraint in a 3D surface.

Figure 2. Determination of ΔH through shadow constraint in 2D and 3D. (a) Determination of ΔH through shadow constraint in a 2D profile. (b) Determination of ΔH through shadow constraint in a 3D surface.

The geometric relationship between the topography and illumination direction can be expressed as

$$\Delta H = d \times \tan(\theta) \tag{6}$$

Equation (6) describes the relationship between the elevation difference ΔH; length of shadow along the illumination direction, d; and illumination altitude angle θ. Here, ΔH represents the difference in elevation between the start and endpoints of a shadow along the illumination direction and thus cannot be negative. d is defined as the length of $x_2 - x_3$, corresponding to the projection of the occlusion and boundary points on the horizontal axis. The illumination altitude angle θ is defined as the angle between the illumination rays and the horizontal axis.

Expanding the 2D profile to a 3D scene, Figure 2(a) illustrates the relationships among the illumination source, surface, and shadow regions. The light source azimuth φ is assumed to be known. Thus, the distance d between the occlusion and boundary points can be calculated using Equation (7):

$$d = \begin{cases} \frac{|x_o - x_b|}{\cos\varphi} \times c_x \\ \frac{|y_o - y_b|}{\cos\varphi} \times c_y \end{cases} (\varphi \neq n \cdot \pi, \quad n \in N) \tag{7}$$

where (x_o, y_o) and (x_b, y_b) are the coordinates of the occlusion and corresponding boundary points in the horizontal and vertical directions, respectively, along the illumination azimuth φ. c_x and c_y are cell sizes in the horizontal and vertical directions, respectively. The component of distance d can be measured, enabling the calculation of d through a standard cosine formulation related to its components. c_x and c_y can help optimize the proposed method to adapt to a variety of images with different resolutions. Substituting Equation (7) into Equation (6), ΔH can be written as

$$\Delta H = |z_o - z_b| = \begin{cases} \frac{|x_o - x_b|}{\cos\varphi} \times c_x \times \tan(\theta) \\ \frac{|y_o - y_b|}{\cos\varphi} \times c_y \times \tan(\theta) \end{cases} .(\varphi \neq n \cdot \pi, n \in N) \quad (8)$$

Equation (8) outlines the shadow constraint for an individual terrain profile. However, ΔH contains two unknown height values: (1) the elevation of the occlusion point z_o and (2) its corresponding boundary point z_b. As the equation only provides one constraint, the system is underdetermined, and a unique solution for ΔH cannot be obtained from a single profile. To address this problem, the proposed method incorporates a coupled optimization approach that jointly treats SfS and shadow constraints, allowing the estimates to be synergistically improved through iterative processing. The reconstruction is incrementally enhanced through the shadow constraint, incorporating multiple NAC images into the SfS process. Regularly updating the elevation and shadow constraint in the illuminated areas facilitates solution convergence. The shadow constraint introduces corrections to optimize the height of the shadow boundary points while fixing the heights of the occlusion points. These corrections are applied to the shadowed regions while retaining the values in the illuminated regions. Therefore, the shadow constraint method for elevations of shaded grids can be expressed as

$$Z_o - Z_{\text{Shadow}} \leq \begin{cases} \frac{|x_o - x_b|}{\cos\varphi} \times c_x \times \tan(\theta) \\ \frac{|y_o - y_b|}{\cos\varphi} \times c_y \times \tan(\theta) \end{cases} .(\varphi \neq n \cdot \pi, n \in N) \quad (9)$$

where Z_o is the elevation of the shadow occlusion point, and Z_{Shadow} represents the elevation of the pixel within the shadow along the illumination direction. The difference in elevation between the shadow boundary point and shadow occlusion point conforms to the equality relationship, while the elevation of interior points is constrained by the inequality relationship.

3.4. Shadow smoothness constraint

The shadow constraint optimizes the DEM by adjusting the elevations of individual terrain profiles, resulting in visible inconsistencies between adjacent profiles. The provided shadow constraint considers constraints only along the direction of illumination and neglects constraints in the perpendicular direction. Thus, an additional constraint is introduced to prevent inconsistencies between adjacent profiles. The proposed shadow smoothness constraint optimizes the elevations along the profile without modifying the profile shape. The shadow smoothness constraint is further weighted and adjusted according to the shaded length of the profiles. The iterative implementation of shadow and smoothness constraints optimizes the reconstruction to yield a coherent solution for the DEM.

As shown in Figure 3, $prf_i^{'}$, $prf_{i-1}^{'}$, and $prf_{i+1}^{'}$ denote the average elevations of the i^{th} profile prf_i and its adjacent profiles prf_{i-1} and prf_{i+1}, respectively. len_{i-1}, len_i, and len_{i+1} represent the distances covered by prf_{i-1}, prf_i, and prf_{i+1}, respectively. The proposed method adjusts the elevations of prf_i according to $prf_{i-1}^{'}$ and $prf_{i+1}^{'}$. d_{i-1} and d_{i+1} denote the average difference in elevation between prf_{i-1} and prf_{i+1}, respectively. d_i is obtained as a weighted average of $prf_{i-1}^{'}$, $prf_{i+1}^{'}$, len_{i-1}, and len_{i+1}. The calculation process is presented in Equation (10) and Equation (11).

$$\begin{cases} d_{i-1} = \overline{prf_{i-1}^{'}} - \overline{prf_i^{'}} \\ d_{i+1} = \overline{prf_{i+1}^{'}} - \overline{prf_i^{'}} \end{cases} \quad (10)$$

$$d_i = \frac{d_{i-1} \times len_{i-1} + d_{i+1} \times len_{i+1}}{len_{i-1} + len_{i+1}} \quad (11)$$

A weighted correction is applied to all shadow profiles in the image, ensuring a constraint between profiles perpendicular to the direction of illumination. This modification eliminates the coarse offsets between profiles, allowing them to satisfy constraints both parallel and perpendicular to the illumination direction.

4. Experimental analysis

4.1. Datasets

Two experimental areas located near the Shackleton Crater at the lunar south pole (Figure 4) were selected for validating the proposed approach. These areas are potential landing sites for NASA's Artemis mission (Peña-Asensio et al. 2024) and the European Space Agency's Lunar Lander mission (De Rosa et al. 2012). At present, no high-resolution DEM (i.e. 1 m/pixel or better) is available to support a detailed landing site evaluation of these areas. The LRO NAC images (0.5–1 m/pixel) have been used to generate DEMs with a resolution of 2 m/pixel at several locations through conventional stereo photogrammetry technology (Rosiek et al. 2013). However, these photogrammetric DEMs exhibit severe problems, e.g. the presence of holes and interpolation defects (Figures 6 and 11) owing to severely shadowed regions at the lunar south pole.

The proposed shadow-constrained SfS approach was used to generate DEMs with a resolution of 1 m/pixel for the two selected areas, using the LRO NAC images as input. These images, representing monocular images with a resolution of 0.5–1 m/pixel, were obtained from the LRO Archive (https://ode.rsl.wustl.edu/moon/.), subjected to ortho-rectification, and sampled to a uniform

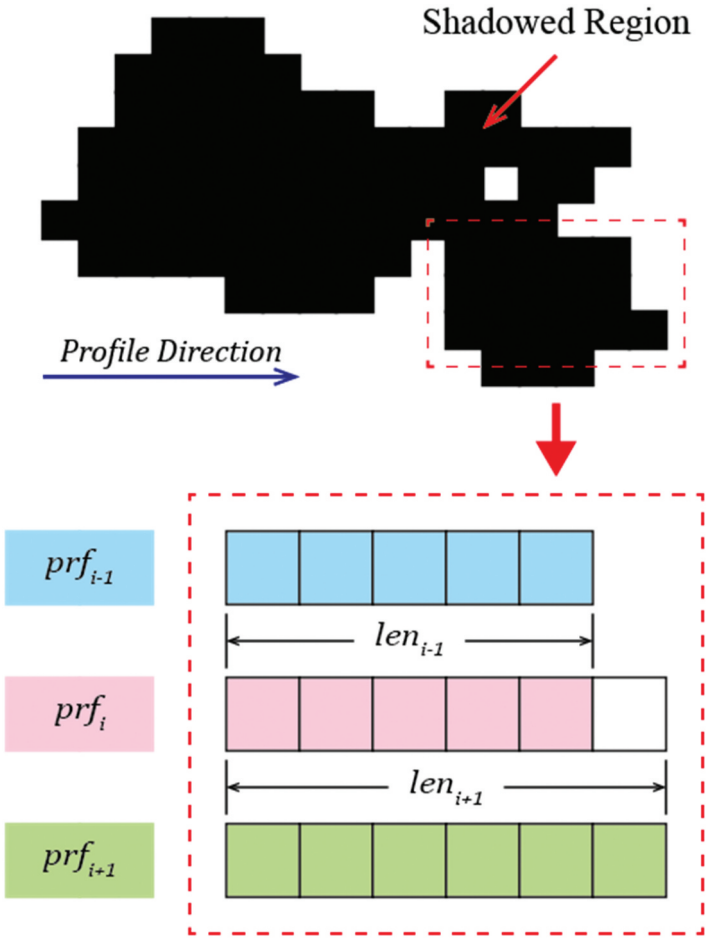

Figure 3. Illustration of the shadow smoothness constraint.

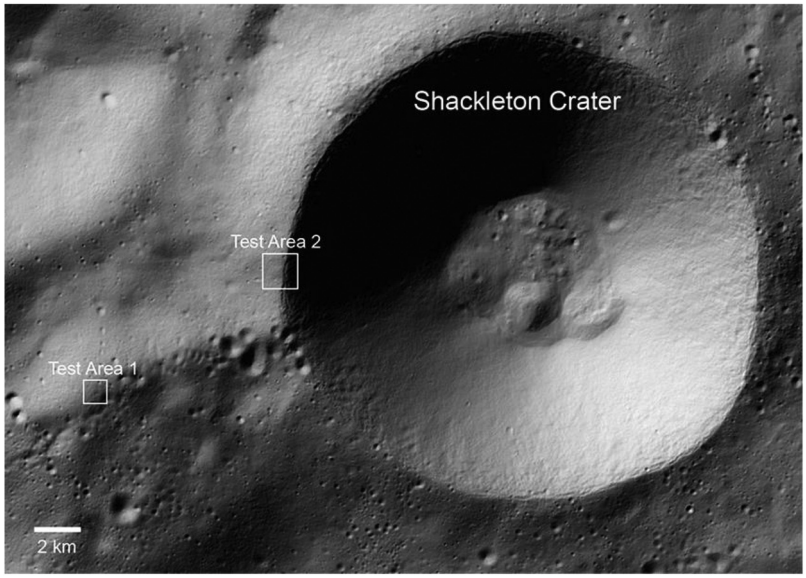

Figure 4. Testing areas in the proximity of the Shackleton Crater at the lunar south pole.

resolution of 1 m/pixel using the ISIS3 software (https://isis.astrogeology.usgs.gov/.) (Laura et al. 2023). A DEM generated from the LRO laser altimeter (LOLA), with a spatial resolution of 20 m/pixel, was used as an initial DEM for the shadow-constrained SfS approach, given the favorable overall geometric accuracy of LOLA DEMs (Mazarico et al. 2011) and their comprehensive coverage of both shadowed and non-shadowed areas. Selected reliable regions on the aforementioned photogrammetric

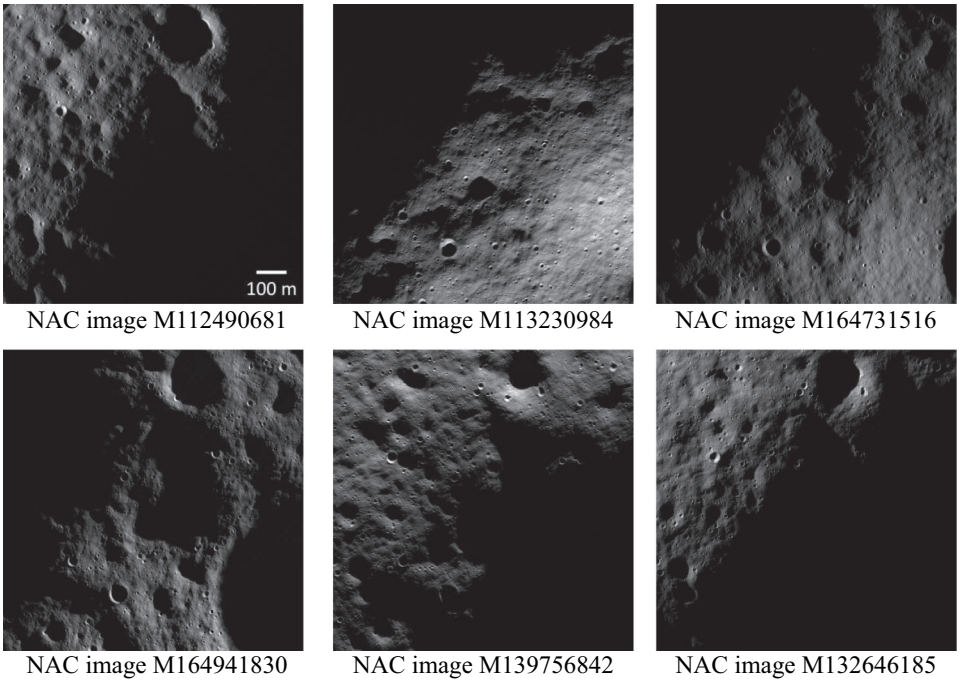

Figure 5. NAC images used for experimental area 1.

Table 1. Information of the NAC images selected for experimental area 1.

Image ID	Resolution (m/pixel)	Incidence angle (°)	Sun azimuth (°)	Image dimension
M139756842	0.850	88.65	14.69	1176 × 1176 pixels
M164941830	0.888	89.84	62.67	1127 × 1127 pixels
M164731516	0.800	89.76	92.19	1250 × 1250 pixels
M113230984	0.832	88.48	157.70	1202 × 1202 pixels
M112490681	0.694	88.99	262.38	1440 × 1440 pixels
M132646185	0.883	89.93	300.00	1132 × 1132 pixels

DEMs (2 m/pixel) were used as references for comparison with the DEMs generated using the proposed shadow-constrained SfS approach.

4.2. Experimental analysis of area 1: connector ridge to Shackleton Crater

The first experimental area is situated at Connector Ridge, a highland ridge connecting with the Shackleton Crater from the southwest (De Rosa et al. 2012; Mazarico et al. 2011). The experimental area covers a region of 1 km × 1 km with the center located at (137.411°W, 89.4679°S). This experimental area features a complex topography, with craters of varying sizes scattered throughout the region. Figure 5 shows the NAC images used for 3D reconstruction, selected for their favorable spatial resolution and varying illumination directions. Details of these NAC images are provided in Table 1. The images were resampled to a uniform resolution of 1 m/pixel to generate a DEM with a resolution of 1 m/pixel using the shadow-constrained SfS approach.

Figure 6 presents a qualitative evaluation, by illustrating the 3D views of the input LOLA DEM (Figure 6(a)), the SfS DEM (Figure 6(b)), the shadow-constrained SfS DEM (Figure 6(c)), and the photogrammetric DEM used as a reference (Figure 6(d)). The NAC image mosaic with maximum illumination is shown in Figure 6(e) as a reference. The small topographic features on the NAC image mosaic are well reconstructed for both the SfS DEM and shadow-constrained SfS DEM. However, several craters (e.g. the lower left corner in Figure 6(b)) are not sufficiently reconstructed in terms of depth in the SfS DEM owing to limited illuminated coverage of the NAC images. The depths of these craters are better reconstructed in the shadow-constrained SfS DEM (also shown in Figure 9).

Figure 7 displays the elevation difference maps between the photogrammetric NAC DEM, used as a reference, and the LOLA DEM, the SfS DEM, and the shadow-constrained SfS DEM, respectively, in a selected local region with the least noise. The DEMs were resampled to a resolution of 2 m/pixel for comparison, matching that of the reference NAC DEM. The LOLA DEM shows considerable elevation differences in the lower-left region (Figure 7(b)). In contrast, these differences were significantly reduced in both the SfS DEM and the shadow-constrained SfS

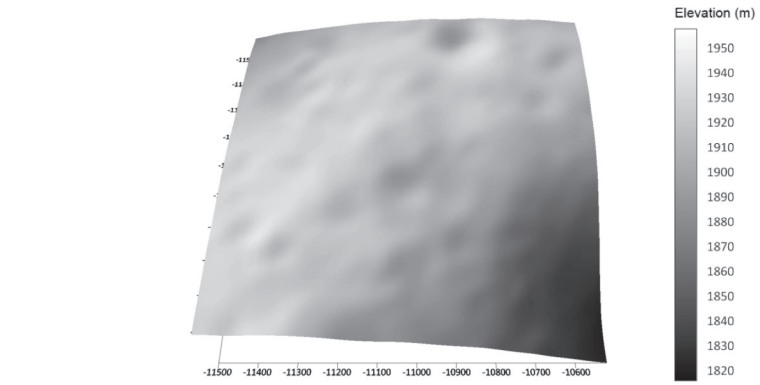

(a) Input LOLA DEM (20 m/pixel)

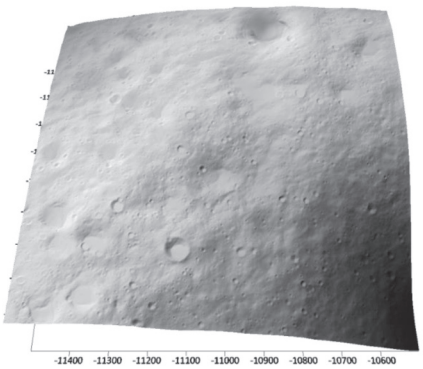

(b) SfS DEM (1 m/pixel)

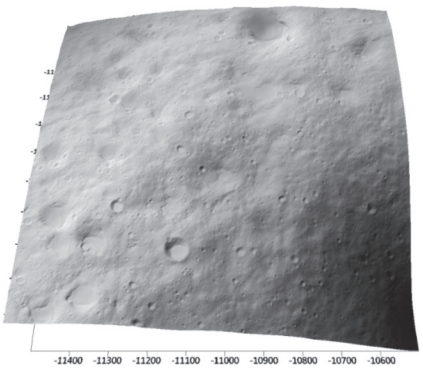

(c) Shadow-constrained SfS DEM (1 m/pixel)

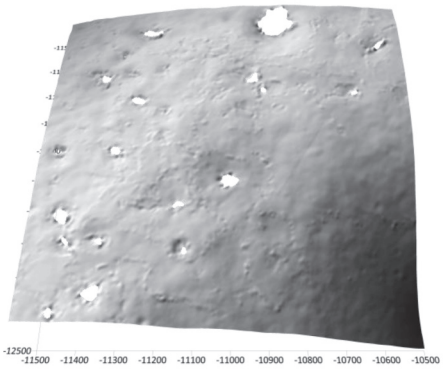

(d) Reference photogrammetric DEM (2 m/pixel) generated from stereo NAC images

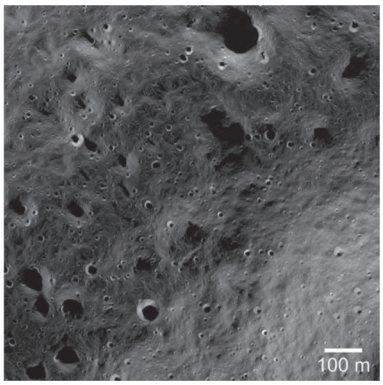

(e) Reference NAC image mosaic with maximum illumination

Figure 6. Experimental area 1: 3D views of the (a) input LOLA DEM, (b) SfS DEM, (c) shadow-constrained SfS DEM, and (d) reference photogrammetric DEM; (e) NAC image mosaic with maximum illumination for reference.

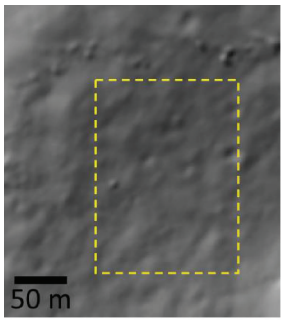

(a) Selected region for comparison.

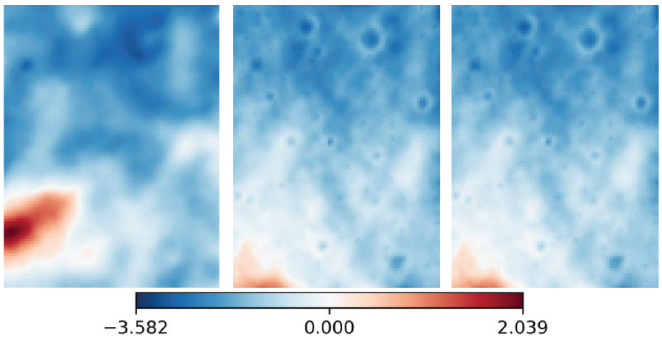

(b) Difference map: Photogrammetric DEM – LOLA DEM

(c) Difference map: Photogrammetric DEM – SfS DEM

(d) Difference map: Photogrammetric DEM – Shadow-constrained SfS DEM

Figure 7. Comparison between the LOLA DEM, SfS DEM, and shadow-constrained SfS DEM with respect to the reference photogrammetric DEM for area 1.

DEM in the same region, which indicates the favorable performance of the SfS approach. Table 2 lists the comparison statistics, including the root mean square error (RMSE) and maximum absolute difference (Max. Abs.) between the DEMs. The RMSE of LOLA DEM (2.03 m) is larger than that of the reference

Table 2. Statistics of comparison between the LOLA DEM, SfS DEM, and shadow-constrained SfS DEM with respect to the reference photogrammetric DEM for area 1.

DEM Types	RMSE (m)	Max. Abs. (m)
LOLA DEM (20 m/pixel)	2.03	3.36
SfS DEM (1 m/pixel)	1.92	3.49
Shadow-constrained SfS DEM (1 m/pixel)	1.91	3.58

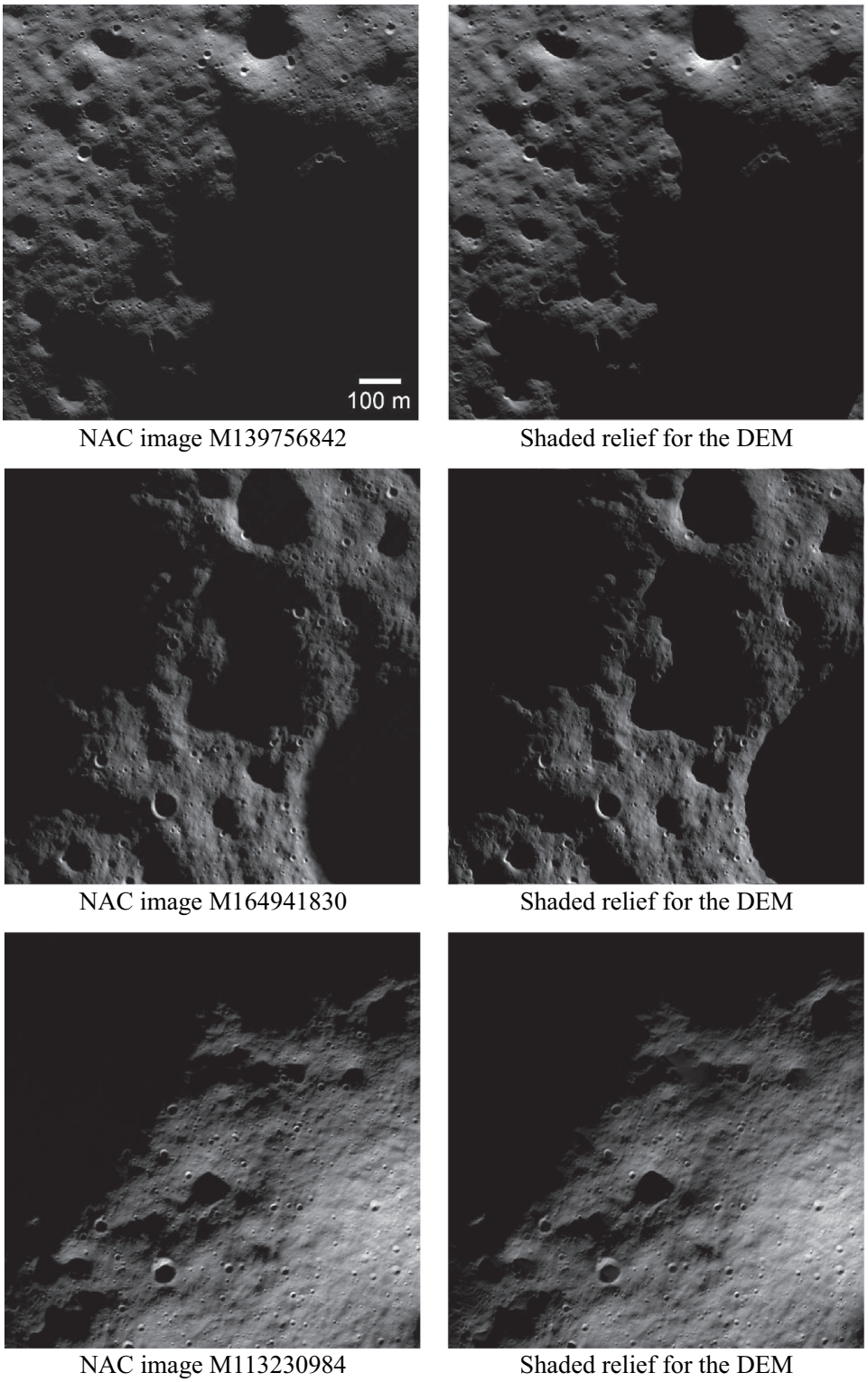

Figure 8. Comparison of NAC images and shaded relief images generated from the shadow-constrained SfS DEM for area 1 under the same solar incidence and azimuth angles.

Table 3. SSIM between the NAC images and shaded relief images generated from the LOLA DEM, SfS DEM, and shadow-constrained SfS DEM for area 1.

	SSIM		
Image ID	LOLA DEM	SfS DEM	Shadow-constrained SfS DEM
M139756842	0.588	0.876	0.885
M164941830	0.590	0.821	0.822
M164731516	0.606	0.909	0.910
M113230984	0.635	0.886	0.887
M112490681	0.731	0.810	0.810
M132646185	0.715	0.884	0.888

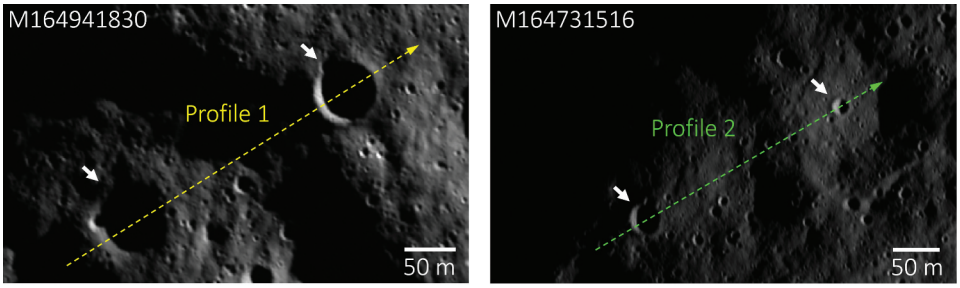

(a) Profiles selected for comparison

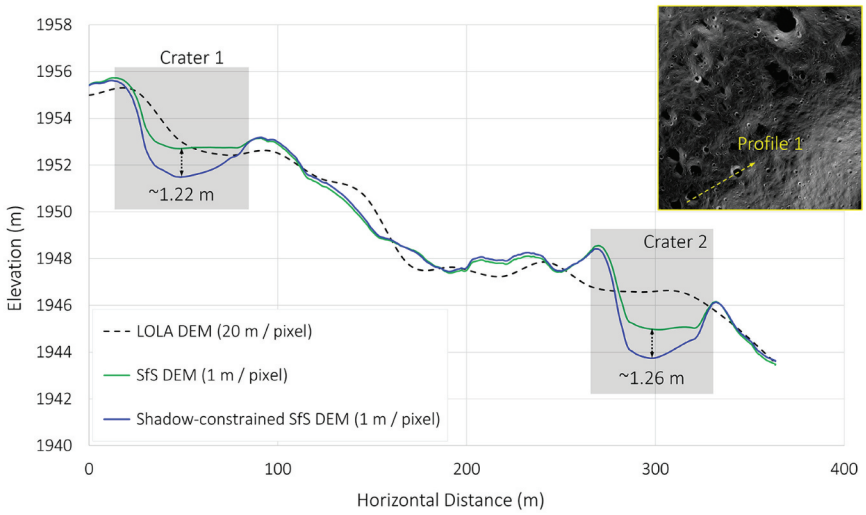

(b) Profile 1

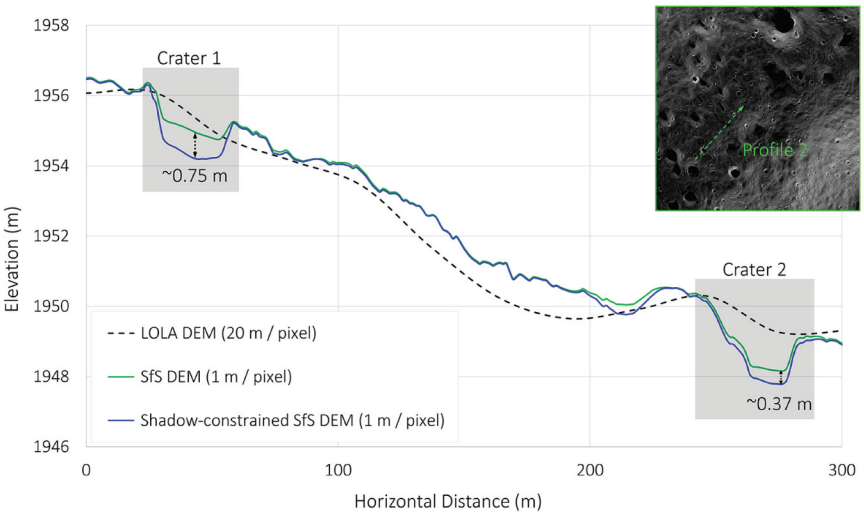

(c) Profile 2

Figure 9. Profile comparison among different DEMs for experimental area 1.

photogrammetric DEM. The RMSE is reduced to 1.92 m for the SfS DEM and 1.91 m for the shadow-constrained SfS DEM. Interestingly, the Max. Abs. increases from 3.36 m for the LOLA DEM to 3.49 m for the SfS DEM and 3.58 m for the shadow-constrained SfS DEM, potentially due to the unsatisfactory quality of the NAC DEM and the SfS DEM in shadow proximity regions, demonstrating the effectiveness of the shadow constraint.

In order to provide a visual evaluation of the reconstructed terrain details, shaded relief images were generated using the shadow-constrained SfS DEM and compared with the actual NAC images. The shaded relief images were produced with the same solar incidence and azimuth angles as those measured when the NAC images were captured. Figure 8 shows examples of side-by-side comparisons of the actual NAC images and the shaded relief images derived from the shadow-constrained SfS DEM. The comparison shows that the shaded relief images are highly consistent with the NAC images, especially in regions along the boundaries of shadows, indicating well-reconstructed elevations along the shadow boundaries.

Table 3 presents quantitative measurements of similarity between NAC images and shaded relief images in terms of the Structural Similarity Index Measure (SSIM). The SSIM, which is calculated considering the image luminance, contrast, and structure (Wang et al. 2004), ranges from −1 to 1, with a larger SSIM indicating higher similarity. Moreover, Table 3 presents the shaded relief images derived from the LOLA DEM and SfS DEM for comparison. As expected, the shaded relief images from the LOLA DEM exhibit the lowest SSIM owing to the sparse resolution. The SSIM values associated with the SfS DEM are significantly improved, highlighting the effectiveness of the SfS algorithm in reconstructing terrain details. The SSIMs of the shadow-constrained SfS DEM are further improved, which can be attributed to improved reconstruction in regions along the shadow boundaries.

Figure 9 presents a detailed comparison of the elevation profiles derived from the LOLA DEM, SfS DEM, and shadow-constrained SfS DEM. Profile 1 crosses two craters, which are absent in the LOLA DEM. In the SfS DEM, the two craters are partially reconstructed, and the concave shapes of the craters

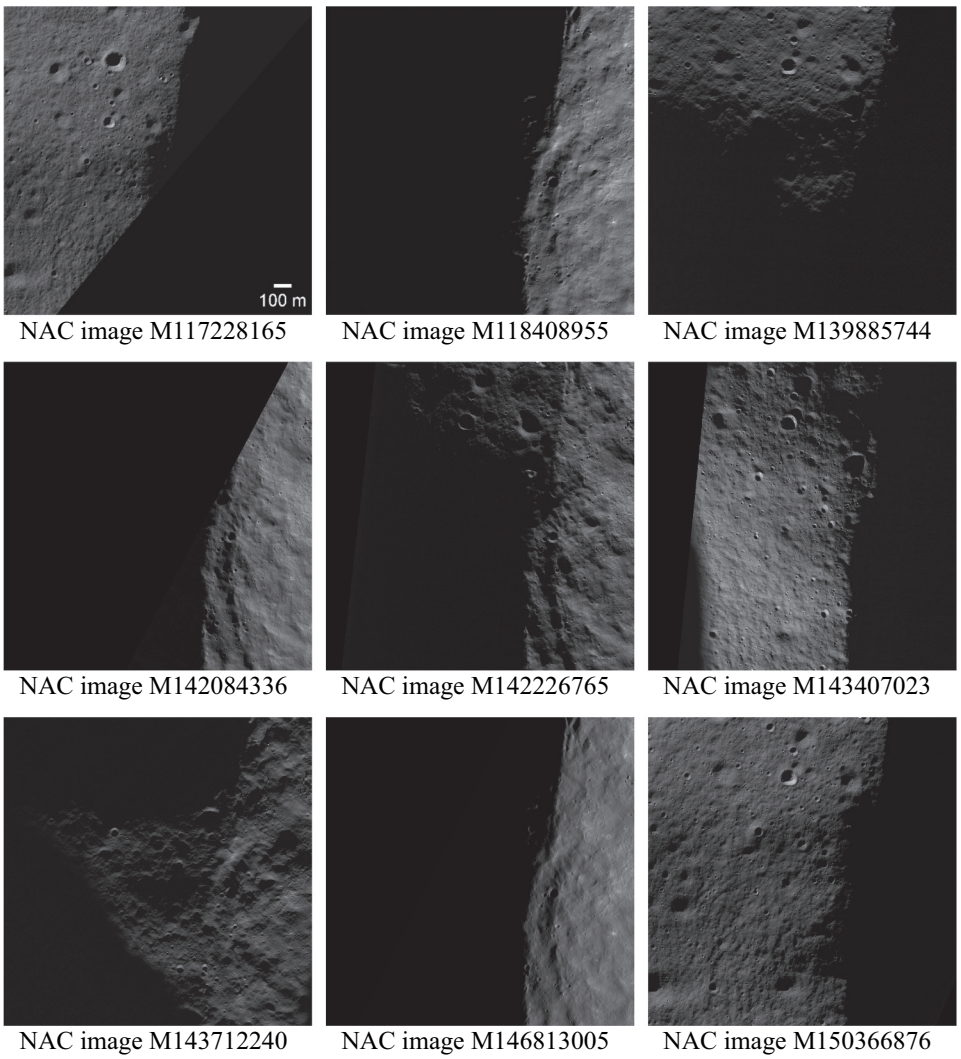

Figure 10. NAC images used for experimental area 2.

Table 4. Information of the NAC images selected for experimental area 2.

Image ID	Resolution (m/pixel)	Incidence angle (°)	Sun azimuth (°)	Image dimension
M117228165	0.656	89.95	313.91	2745 × 2745 pixels
M118408955	0.892	90.00	149.08	2017 × 2017 pixels
M139885744	0.763	88.65	356.43	2359 × 2359 pixels
M142084336	0.876	88.69	45.97	2055 × 2055 pixels
M142226765	0.745	88.73	26.21	2416 × 2416 pixels
M143407023	0.771	88.58	219.94	2334 × 2334 pixels
M143712240	0.885	88.61	176.71	2034 × 2034 pixels
M146813005	0.863	89.64	100.11	2086 × 2086 pixels
M150366876	0.688	90.95	320.33	2616 × 2616 pixels

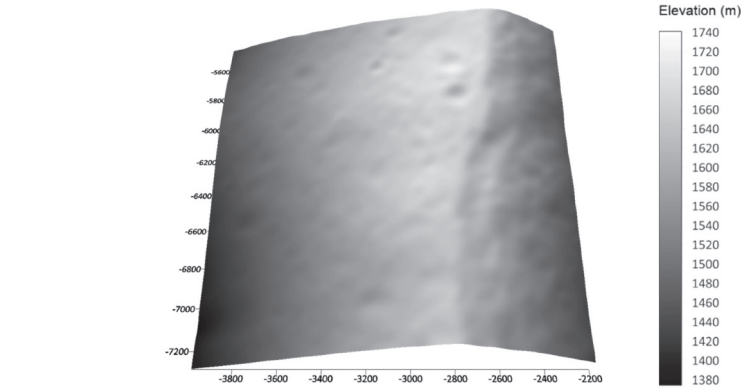

a) Input LOLA DEM (20 m/pixel)

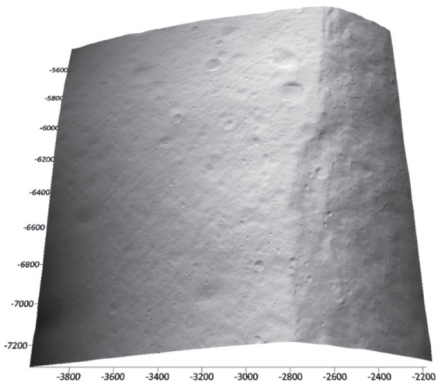

(b) SfS DEM (1 m/pixel)

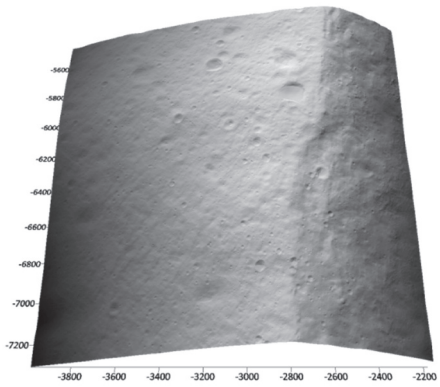

(c) Shadow-constrained SfS DEM (1 m/pixel)

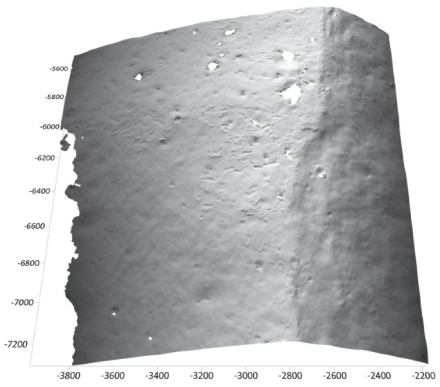

(d) Reference photogrammetric DEM (2 m/pixel) generated from stereo NAC images

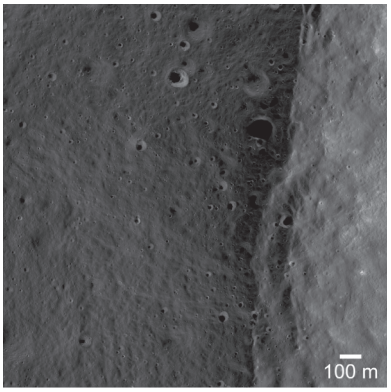

(e) Reference NAC image mosaic with maximum illumination

Figure 11. Experimental area 2: 3D views of the (a) input LOLA DEM, (b) SfS DEM, (c) shadow-constrained SfS DEM, and (d) reference photogrammetric DEM; (e) NAC image mosaic with maximum illumination for reference.

can be observed. However, in the shadowed regions within the craters, only flat terrains are reconstructed. In the shadow-constrained SfS DEM, the craters are better reconstructed, with depths increased by ~1.22 m and 1.26 m for the two craters. Given that the two craters have a diameter of approximately 50 m, their

appropriate depths are expected to be at least 3 m, considering average depth-to-diameter ratios of 0.06–0.16 for lunar craters (Wu et al. 2022). Therefore, the shadow-constrained SfS DEM yields more reasonable results than the SfS DEM. Similar results can be observed from the comparison of profile 2. These profile comparisons demonstrate that the shadow-constrained SfS approach not only can reconstruct small terrain features but also yield more reasonable geometric information.

4.3. Experimental analysis of area 2: eastern rim of Shackleton Crater

Experimental area 2 is located on the eastern rim of the Shackleton Crater, with complex illumination conditions and limited illumination coverage in the peak region of the rim. This experimental area covers a region of 1.8 km × 1.8 km, with the center located at (−143.651°W, −89.826°S). Figure 10 shows the NAC images used for 3D reconstruction, with corresponding details presented in Table 4.

Figure 11 presents the results of the qualitative evaluation by illustrating the 3D views of the input LOLA DEM (Figure 11(a)), the SfS DEM (Figure 11(b)), the shadow-constrained SfS DEM (Figure 11(c)), and the photogrammetric DEM used for reference (Figure 11(d)). The photogrammetric DEM exhibits obvious defects on the right side of the crater rim, which are attributable to data interpolation in these regions lacking data. The NAC image mosaic with maximum illumination is shown in Figure 11(e) for reference. The small topographic features in the NAC image mosaic are well reconstructed on both the SfS DEM and shadow-constrained SfS DEM.

To quantitatively evaluate the derived DEMs, we generated elevation difference maps between the photogrammetric NAC DEM and the LOLA DEM, the SfS DEM, and the shadow-constrained SfS DEM, respectively, in a selected local region with minimal noise. The most significant differences were observed in the craters on the LOLA DEM in the center-left region (Figure 12(b)) because the LOLA DEM did not fully capture the terrain details. The differences in the SfS DEM and shadow-constrained SfS DEM are reduced, indicating that the SfS methods successfully reconstructed the topographic details. Table 5 lists the corresponding comparison statistics. The overall RMSE of the shadow-constrained SfS DEM is 1.08 m, which is lower than that of the SfS DEM (1.09 m) and the LOLA DEM (1.10 m). The maximum absolute difference for the LOLA DEM is 3.15 m, which is higher than those of the SfS DEM and shadow-constrained SfS DEM, indicating that the proposed method is effective in reconstructing more reliable elevations in shadowed regions.

Figure 13 shows examples of side-by-side comparisons of the actual NAC images and shaded relief images generated from the shadow-constrained SfS DEM for area 2, revealing high visual consistency between the two types of images. Table 6 summarizes the SSIMs between the NAC images and shaded relief images generated from the LOLA DEM, SfS DEM, and shadow-constrained SfS DEM. The shaded relief images from the shadow-constrained SfS DEM exhibit higher SSIMs than those associated with the LOLA DEM and SfS DEM.

Figure 14 presents a detailed comparison of the elevation profiles derived from the LOLA DEM, the SfS DEM, and the shadow-constrained SfS DEM. In this test area, the high density of LOLA measurements (laser-measured points) allows us to include them for direct comparison. Profile 1 crosses a group of craters. The profile from the LOLA DEM only depicts the crater with a relatively larger diameter, while the others are absent. In both profiles from the SfS DEM and the shadow-constrained SfS DEM, the four craters are reconstructed, with the latter presenting deeper depths and higher consistency with the LOLA points,

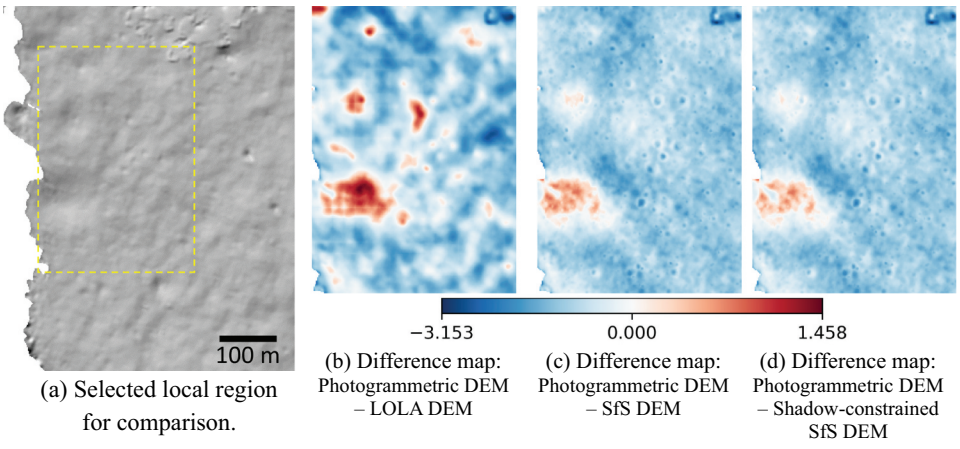

(a) Selected local region for comparison.

(b) Difference map: Photogrammetric DEM – LOLA DEM

(c) Difference map: Photogrammetric DEM – SfS DEM

(d) Difference map: Photogrammetric DEM – Shadow-constrained SfS DEM

Figure 12. Comparison between the LOLA DEM, SfS DEM, and shadow-constrained SfS DEM with respect to the reference photogrammetric DEM for area 2.

Table 5. Statistics of comparison between the LOLA DEM, SfS DEM, and shadow-constrained SfS DEM with respect to the reference photogrammetric DEM for area 2.

DEM Types	RMSE (m)	Max. Abs. (m)
LOLA DEM (20 m/pixel)	1.10	3.15
SfS DEM (1 m/pixel)	1.09	3.09
Shadow-constrained SfS DEM (1 m/pixel)	1.08	3.09

especially at the crater floors and rims. This indicates that the shadow-constrained SfS performs better than the classical SfS method. Profile 2 is located at the rim of Shackleton Crater and crosses through two craters. Both the SfS DEM and the shadow-constrained SfS DEM successfully reconstruct the small-scale topographical details, such as crater rims and floors, not

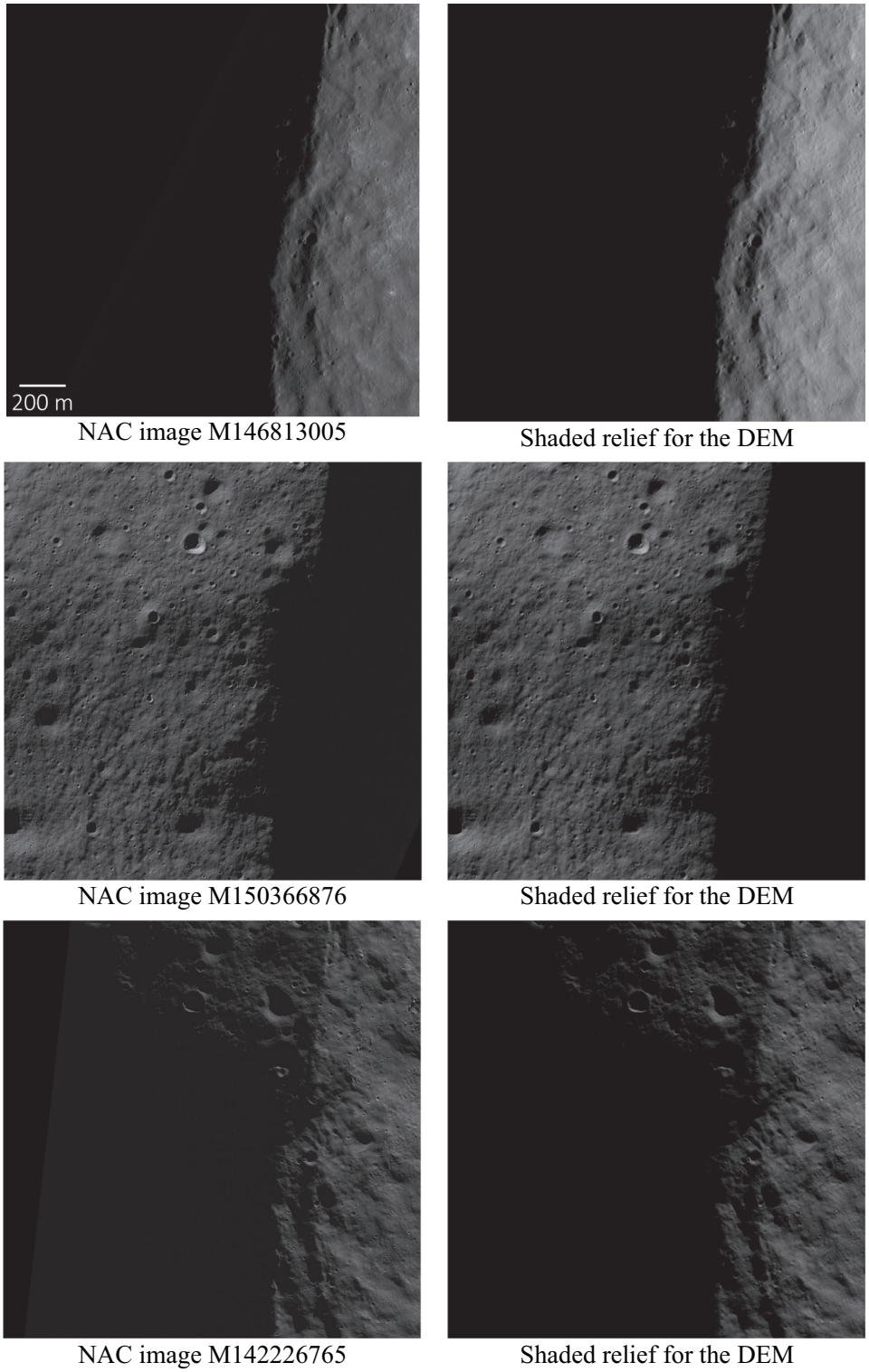

Figure 13. Comparison of NAC images and shaded relief images generated from the shadow-constrained SfS DEM for area 2 under the same solar incidence and azimuth angles.

Table 6. SSIM between the NAC images and shaded relief images generated from LOLA DEM, SfS DEM, and shadow-constrained SfS DEM for area 2.

	SSIM		
Image ID	LOLA DEM	SfS DEM	Shadow-constrained SfS DEM
M117228165	0.335	0.825	0.846
M118408955	0.651	0.843	0.857
M139885744	0.648	0.862	0.885
M142084336	0.673	0.920	0.922
M142226765	0.618	0.804	0.834
M143407023	0.479	0.831	0.839
M143712240	0.501	0.799	0.820
M146813005	0.674	0.870	0.875
M150366876	0.358	0.806	0.837

captured by the LOLA DEM. However, the profile from the shadow-constrained SfS DEM better matches the direct LOLA measurements, again demonstrating the advantage of the shadow constraint.

5. Conclusions and discussion

This paper presents a shadow-constrained SfS method for pixel-wise 3D surface reconstruction at the lunar south pole. The performance of the proposed approach is evaluated using actual LRO NAC images of two areas

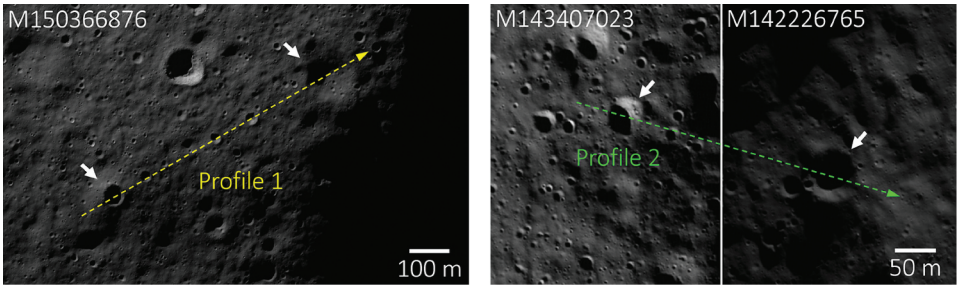

(a) Profiles selected for comparison

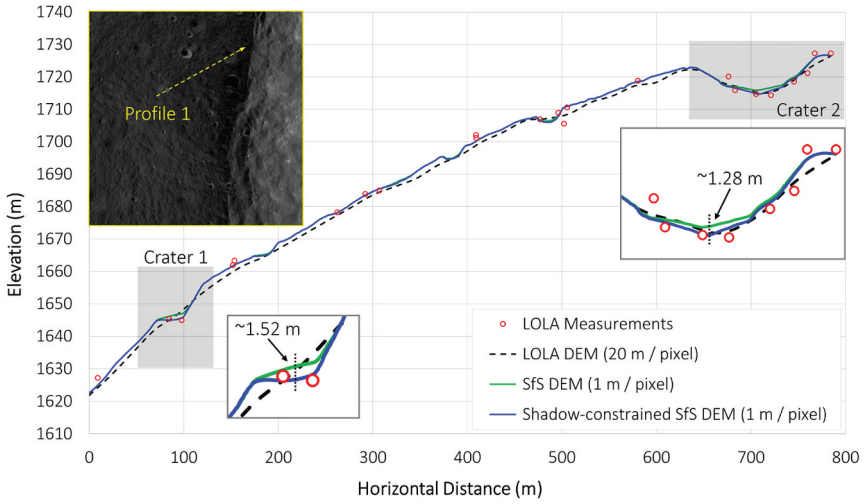

(b) Profile 1

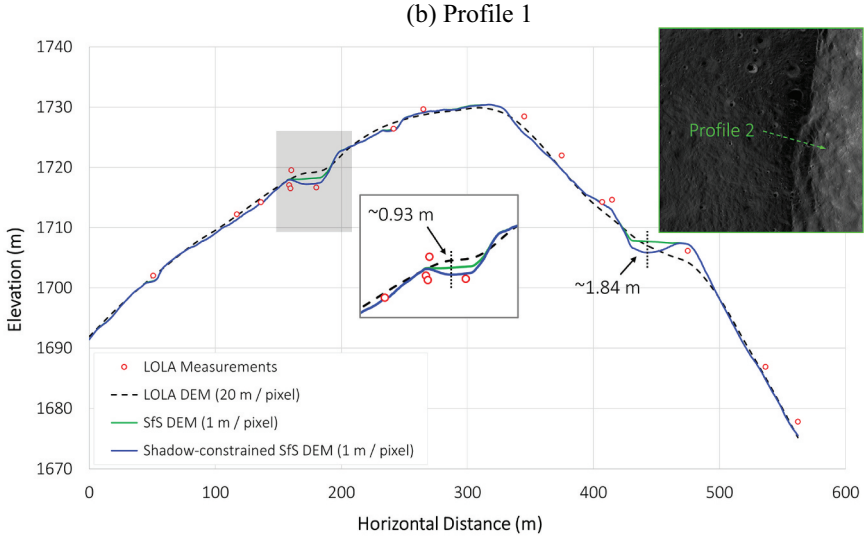

(c) Profile 2

Figure 14. Profile comparison among the DEMs for experimental area 2.

at the lunar south pole. The experimental results reveal that the proposed approach can yield high-resolution DEMs that have the same resolution as the input NAC images and are characterized by subtle topographic details and favorable geometric accuracy. Comparisons with the photogrammetric DEM generated from stereo NAC images show that the shadow-constrained SfS DEM exhibits lower RMSEs than those of the LOLA DEM and SfS DEM. The similarity between the actual LRO NAC images and shaded relief images generated from the shadow-constrained SfS DEM is significantly improved compared to those of images rendered from the LOLA DEM and SfS DEM. Detailed profile comparisons and comparison with the direct LOLA points further validate the effectiveness of the shadow constraint in optimizing 3D reconstruction in regions in proximity to shadows and within the shadows.

Notably, the shadow constraint may not be effective in addressing the effects of indirect reflectance proximity to the boundaries of shadows and challenging illumination conditions induced by occlusions at a distance. However, the proposed shadow-constrained SfS method presented herein can enable detailed 3D surface reconstruction at the lunar south pole. The proposed method can be used to generate high-resolution DEMs to support future missions for exploring the lunar south pole, with applications including landing site evaluation, route planning for lunar probes or astronauts. The generated high-resolution DEMs can also facilitate geomorphological and geological analyses of the region, studying the small-scale surface roughness or the influence of possible ground ice on the relief.

Disclosure statement

No potential conflict of interest was reported by the author(s).

Funding

This work was supported by grants from the Research Grants Council of Hong Kong [grant numbers: R5043-19, PolyU 15219821, PolyU 15215822].

Notes on contributors

Ranye Jia received the B.S. degree in remote sensing from Capital Normal University, Beijing, China, in 2020. He is currently pursuing the Ph.D. degree with a major in planetary remote sensing and mapping with the Hong Kong Polytechnic University. His research interests include planetary mapping, photometry, and shape-from-shading.

Bo Wu is a Professor with the Department of Land Surveying and Geo-Informatics, the Hong Kong Polytechnic University. His research interests are mainly in planetary remote sensing and robotic vision. He chairs the ISPRS Working Group "Planetary Remote Sensing and Mapping" and serves as Associate Editor or Editorial Board Member of several international journals.

Wai Chung Liu received his Ph.D. degree from the Hong Kong Polytechnic University in 2020. He is currently an Associate Professor at the Aerospace Information Research Institute, Chinese Academy of Sciences. His research interests include planetary mapping, photometry, and related scientific applications.

Yue Peng received her B.S. degree in remote sensing from Shandong University of Science and Technology, China, in 2020. She is currently a Research Assistant at the Hong Kong Polytechnic University. Her research interests are mainly in planetary mapping.

Sergey Krasilnikov received his Ph.D. degree from Moscow State University, Russia, in 2021. He is currently a Research Assistant Professor with the Department of Land Surveying and Geo-Informatics, the Hong Kong Polytechnic University. His research interests are mainly in planetary geology and geomorphology.

Liyan Sheng is a System Designer with the China Academy of Space Technology, P.R. China. Her research interests are mainly in spacecraft engineering and planetary mapping.

Song Peng is a Senior System Designer with the China Academy of Space Technology, P.R. China. His research interests are mainly in spacecraft engineering and planetary mapping.

ORCID

Ranye Jia http://orcid.org/0009-0000-3018-4603
Bo Wu http://orcid.org/0000-0001-9530-3044
Wai Chung Liu http://orcid.org/0000-0003-3865-0714
Sergey Krasilnikov http://orcid.org/0000-0002-5023-3908

Data availability statement

The LRO NAC images that support the findings of this study are publicly available from the LRO Archive (https://ode.rsl.wustl.edu/moon/). The photogrammetric DEM used as a reference for comparison analysis can be downloaded from the USGS website (https://astrogeology.usgs.gov/search/map/Moon/LRO/MOON_LRO_NAC_DEM_89S210E_4mp).

References

Alexandrov, O., and R. A. Beyer. 2018. "Multiview Shape-From-Shading for Planetary Images." *Earth & Space Science* 5 (10): 652–666.

Chandraker, M., S. Agarwal, and D. Kriegman. 2007. "Shadowcuts: Photometric Stereo with Shadows". *2007 IEEE Conference on Computer Vision and Pattern Recognition*, Minneapolis, MN, 1–8. IEEE.

Chen, H., X. Hu, P. Gläser, H. Xiao, Z. Ye, H. Zhang, X. Tong, and J. Oberst. 2022. "CNN-Based Large Area Pixel-Resolution Topography Retrieval from Single-View LROC NAC Images Constrained with SLDEM." *IEEE Journal of Selected Topics in Applied Earth Observations & Remote Sensing* 15:9398–9416. https://doi.org/10.3390/rs13050839.

Chen, Z., B. Wu, and W. C. Liu. 2021. "Mars3DNet: CNN-Based High-Resolution 3D Reconstruction of the Martian Surface from Single Images." *Remote Sensing* 13 (5): 839.

Daum, M., and G. Dudek. 1998. "On 3-D Surface Reconstruction Using Shape from Shadows." *Proceedings. 1998 IEEE Computer Society conference on computer vision and pattern recognition (Cat. No. 98CB36231)*, Santa Barbara, CA, 461–468. IEEE.

De Rosa, D., B. Bussey, J. T. Cahill, T. Lutz, I. A. Crawford, T. Hackwill, S. van Gasselt, et al. 2012. "Characterisation of Potential Landing Sites for the European Space Agency's Lunar Lander Project." *Planetary & Space Science* 74 (1): 224–246.

Di, K., Y. Liu, B. Liu, M. Peng, and W. Hu. 2014. "A Self-Calibration Bundle Adjustment Method for Photogrammetric Processing of Chang'E-2 Stereo Lunar Imagery." *IEEE Transactions on Geoscience and Remote Sensing* 52 (9): 5432–5442. https://doi.org/10.1109/TGRS.2013.2288932.

Dulova, I. A., S. I. Skuratovsky, N. V. Bondarenko, and Y. V. Kornienko. 2008. "Reconstruction of the Surface Topography from Single Images with the Photometric Method." *Solar System Research* 42:522–535. https://doi.org/10.1134/S0038094608060051 .

Gaskell, R. W. 2004. "High Resolution Shape and Topography of Eros-Preliminary Results from NEAR Imaging Data." *AGU Spring Meeting Abstracts*, Montreal, Quebec. (Vol. 2004, P33C–06).

Gaskell, R. W., O. S. Barnouin-Jha, D. J. Scheeres, A. S. Konopliv, T. Mukai, S. Abe, J. Saito, et al. 2008. "Characterizing and Navigating Small Bodies with Imaging Data." *Meteoritics & Planetary Science* 43 (6): 1049–1061.

Grumpe, A., F. Belkhir, and C. Wöhler. 2014. "Construction of Lunar DEMs Based on Reflectance Modelling." *Advances in Space Research* 53 (12): 1735–1767.

Heipke, C., J. Oberst, J. Albertz, M. Attwenger, P. Dorninger, E. Dorrer, M. Ewe, et al. 2007. "Evaluating Planetary Digital Terrain Models—The HRSC DTM Test." *Planetary & Space Science* 55 (14): 2173–2191.

Hess, M., M. Tenthoff, K. Wohlfarth, and C. Wöhler. 2022. "Atmospheric Correction for High-Resolution Shape from Shading on Mars." *Journal of Imaging* 8 (6): 158.

Horn, B. K. P. 1977. "Understanding Image Intensities." *Artificial Intelligence* 8 (2): 201–231.

Horn, B. K. P. 1990. "Height and Gradient from Shading." *International Journal of Computer Vision* 5 (1): 37–75.

Kirk, R. L. 1987. "A Fast Finite-Element Algorithm for Two-Dimensional Photoclinometry." PhD diss., California Institute of Technology.

Korokhin, V., Y. Velikodsky, Y. Shkuratov, V. Kaydash, U. Mall, and G. Videen. 2018. "Using LROC WAC Data for Lunar Surface Photoclinometry." *Planetary & Space Science* 160:120–135. https://doi.org/10.1016/j.pss.2018.05.020.

Laura, J., A. Acosta, T. Addair, L. Adoram-Kershner, J. Alexander, O. Alexandrov, and S. Alley. 2023. "Integrated Software for Imagers and Spectrometers, v7.2.0_RC1." *Zenodo*. https://doi.org/10.5281/zenodo.7644616 .

Li, Z., B. Wu, W. C. Liu, and Z. Chen. 2021. "Integrated Photogrammetric and Photoclinometric Processing of Multiple HRSC Images for Pixelwise 3-D Mapping on Mars." *IEEE Transactions on Geoscience & Remote Sensing* 60:1–13. https://doi.org/10.1109/TGRS.2021.3106737 .

Liu, W. C., and B. Wu. 2020. "An Integrated Photogrammetric and Photoclinometric Approach for Illumination-Invariant Pixel-Resolution 3D Mapping of the Lunar Surface." *Isprs Journal of Photogrammetry & Remote Sensing* 159:153–168. https://doi.org/10.1016/j.isprsjprs.2019.11.017.

Liu, W. C., and B. Wu. 2023. "Atmosphere-Aware Photoclinometry for Pixel-Wise 3D Topographic Mapping of Mars." *Isprs Journal of Photogrammetry & Remote Sensing* 204:237–256. https://doi.org/10.1016/j.isprsjprs.2023.09.017.

Liu, W. C., B. Wu, and C. Wöhler. 2018. "Effects of Illumination Differences on Photometric Stereo Shape-And-Albedo-From-Shading for Precision Lunar Surface Reconstruction." *Isprs Journal of Photogrammetry & Remote Sensing* 136:58–72. https://doi.org/10.1016/j.isprsjprs.2017.12.010.

Liu, Y., Y. Wang, K. Di, M. Peng, W. Wan, and Z. Liu. 2022. "A Generative Adversarial Network for Pixel-Scale Lunar DEM Generation from High-Resolution Monocular Imagery and Low-Resolution DEM." *Remote Sensing* 14 (21): 5420.

Lohse, V., and C. Heipke. 2004. "Multi-Image Shape-From-Shading: Derivation of Planetary Digital Terrain Models Using Clementine Images." *International Archives of the Photogrammetry, Remote Sensing and Spatial Information Sciences - ISPRS Archives* 35:828–833. http://www.scopus.com/inward/record.url?scp=84874435900&partnerID=8YFLogxK.

Mamassian, P. 2014. "Shape from Shadows." In *Computer Vision: A Reference Guide*, edited by K. Ikeuchi, 724–725. Boston, MA: Springer US.

Mazarico, E., G. A. Neumann, D. E. Smith, M. T. Zuber, and M. H. Torrence. 2011. "Illumination Conditions of the Lunar Polar Regions Using LOLA Topography." *Icarus* 211 (2): 1066–1081.

McEwen, A. S. 1991. "Photometric Functions for Photoclinometry and Other Applications." *Icarus* 92 (2): 298–311.

Palmer, E. E., J. N. Head, R. W. Gaskell, M. V. Sykes, and B. McComas. 2016. "Mercator—Independent Rover Localization Using Stereophotoclinometry and Panoramic Images." *Earth & Space Science* 3 (12): 488–509.

Peña-Asensio, E., J. Sutherland, P. Tripathi, K. Mason, A. Goodwin, V. T. Bickel, and D. A. Kring. 2024. "Automated Astronaut Traverses with Minimum Metabolic Workload: Accessing Permanently Shadowed Regions Near the Lunar South Pole." *Acta Astronautica* 214:324–342. https://doi.org/10.1016/j.actaastro.2023.10.010.

Rosiek, M. R., O. Thomas, E. Howington-Kraus, and E. Foster. 2013. "Lunar South Pole Digital Elevation Models from Lunar Reconnaissance Orbiter Narrow Angle Camera." *44th Annual Lunar and Planetary Science Conference*, The Woodlands, TX. (Vol. 1719, p. 2583).

Shafer, S. A., and T. Kanade. 1983. "Using Shadows in Finding Surface Orientations." *Computer Vision, Graphics and Image Processing* 22 (1): 145–176.

Smith, D. E., M. T. Zuber, G. B. Jackson, J. F. Cavanaugh, G. A. Neumann, H. Riris, X. Sun, et al. 2010. "The Lunar Orbiter Laser Altimeter Investigation on the Lunar Reconnaissance Orbiter Mission." *Space Science Reviews* 150:209–241. https://doi.org/10.1007/s11214-009-9512-y .

Speyerer, E. J., R. V. Wagner, M. S. Robinson, A. Licht, P. C. Thomas, K. Becker, J. Anderson, S. M. Brylow, D. C. Humm, and M. Tschimmel. 2016. "Pre-Flight and

On-Orbit Geometric Calibration of the Lunar Reconnaissance Orbiter Camera." *Space Science Reviews* 200:357–392. https://doi.org/10.1007/s11214-014-0073-3.

Tao, Y., P. Muller, S. J. Conway, S. Xiong, S. Walter, and B. Liu. 2023. "Large Area High-Resolution 3D Mapping of the Von Kármán Crater: Landing Site for the Chang'E-4 Lander and Yutu-2 Rover." *Remote Sensing* 15 (10): 2643.

Tran, T., M. R. Rosiek, R. A. Beyer, S. Mattson, E. Howington-Kraus, M. S. Robinson, B. A. Archinal, K. Edmundson, D. Harbour, and E. Anderson. 2010. "Generating Digital Terrain Models Using LROC NAC Images." *Proceedings of the ISPRS Technical Commission IV Conference*, Orlando, Florida. http://www.lpi.usra.edu/meetings/lpsc2010/pdf/2515.pdf.

Tsai, P.-S., and M. Shah. 1994. "Shape from Shading Using Linear Approximation." *Image and Vision Computing* 12 (8): 487–498.

Wang, Z., A. C. Bovik, H. R. Sheikh, and E. P. Simoncelli. 2004. "Image Quality Assessment: From Error Visibility to Structural Similarity." *IEEE Transactions on Image Processing* 13 (4): 600–612. https://doi.org/10.1109/TIP.2003.819861.

Woodham, R. J. 1980. "Photometric Method for Determining Surface Orientation from Multiple Images." *Optical Engineering* 19 (1): 139–144.

Wu, B., H. Hu, and J. Guo. 2014. "Integration of Chang'E-2 Imagery and LRO Laser Altimeter Data with a Combined Block Adjustment for Precision Lunar Topographic Modeling." *Earth and Planetary Science Letters* 391:1–15. https://doi.org/10.1016/j.epsl.2014.01.023.

Wu, B., F. Li, H. Hu, Y. Zhao, Y. Wang, P. Xiao, Y. Li, et al. 2020. "Topographic and Geomorphological Mapping and Analysis of the Chang'E-4 Landing Site on the Far Side of the Moon." *Photogrammetric Engineering & Remote Sensing* 86 (4): 247–258.

Wu, B., Y. Li, W. C. Liu, Y. Wang, Y. Li, F. Zhao, and H. Zhang. 2021. "Centimeter-Resolution Topographic Modeling and Fine-Scale Analysis of Craters and Rocks at the Chang'E-4 Landing Site." *Earth and Planetary Science Letters* 553:116666. https://doi.org/10.1016/j.epsl.2020.116666.

Wu, B., and W. C. Liu. 2017. "Calibration of Boresight Offset of LROC NAC Imagery for Precision Lunar Topographic Mapping." *Isprs Journal of Photogrammetry & Remote Sensing* 128:372–387. https://doi.org/10.1016/j.isprsjprs.2017.04.012.

Wu, B., W. C. Liu, A. Grumpe, and C. Wöhler. 2018. "Construction of Pixel-Level Resolution DEMs from Monocular Images by Shape and Albedo from Shading Constrained with Low-Resolution DEM." *Isprs Journal of Photogrammetry & Remote Sensing* 140:3–19. https://doi.org/10.1016/j.isprsjprs.2017.03.007.

Wu, B., Y. Wang, S. C. Werner, N. C. Prieur, and Z. Xiao 2022. "A Global Analysis of Crater Depth/Diameter Ratios on the Moon." *Geophysical Research Letters* 49 (20): e2022GL100886. https://doi.org/10.1029/2022GL100886.

Wu, B., Y. Zhang, and Q. Zhu. 2012. "Integrated Point and Edge Matching on Poor Textural Images Constrained by Self-Adaptive Triangulations." *Isprs Journal of Photogrammetry & Remote Sensing* 68:40–55. https://doi.org/10.1016/j.isprsjprs.2011.12.005.